Influence of mining geometry on mine hydro-geo-mechanics

M. Bai and D. Elsworth

Abstract — *The influence of mining on the hydro-geo-mechanical environment can be greatly modified by alternating mining geometries. The limiting magnitudes of surface subsidence and groundwater flow over the mining area, as a result of mine geometric changes, can be reasonably predicted through the coupled finite-element model introduced in this paper. The model has been verified using real and conceptual case studies which reveal that changes in strata conductivities are strongly related to the strata deformation induced by mining. The greatest modification of hydraulic conductivities occurs within the caving or severely fractured zones. The study indicates that narrowing the panel face width will substantially reduce both the intensity and extent of mining damage to the overlying strata, limit surface subsidence and constrain the change in hydraulic conductivity to a reduced scale and smaller extent, particularly as mining depth increases.*

Introduction

High productivity longwall mining is becoming increasingly popular for mining uninterrupted and flat lying coal seams. Despite high productivity, the longwall mining is subject to problems related to subsidence and aquifer dewatering. Other researchers have investigated the flow regimes present around underground mines (Owili-Eger, 1975; Booth, 1984) using numerical methods. Of interest is modeling the post-mining hydraulic regime that develops with the changing stress and displacement in strata. Fluid flow and solid deformation develop in a transient manner as compressive and tensile stresses coupled with undrained fluid pressures in response to the migrating face. This transient behavior has been reported by Walker (1988) as illustrated in Fig. 1. Frequently, the effect of the ultimate displacement field induced by mining on affected structures becomes apparent. To address these problems, and to examine the alternative of mining with narrow and less disruptive panels, the following analysis is completed.

Finite-element modeling (FEM)

A finite-element model is developed to represent permeability enhancement in deforming strata containing natural fractures. Deformations throughout the elastic body induce changes in aperture of individual fractures that may drastically change permeability distributions.

The following model is restricted to a two-dimensional configuration within linear elastic fluid saturated media. Governing equations are developed to represent the deformation and flux fields resulting from applied boundary conditions. The equations are subsequently cast in a finite-element format and coupled to represent the steady state response due to mining.

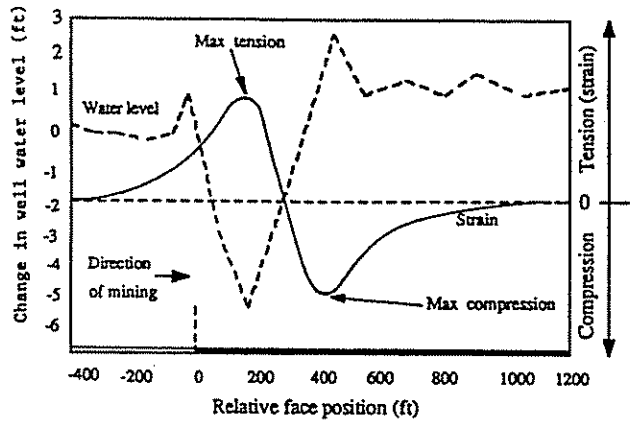

Fig. 1 — Water level fluctuation and ground strain (after Walker, 1988).

Substitution of the strain-stress relation into an equilibrium relation yields the governing equation for the solid phase. Similarly, substitution of Darcy's velocity into a continuity relation, assuming steady state conditions, gives the governing equation for the fluid phase.

The governing equations for both the solid and fluid phases may be developed into a variational statement where the displacement (u) and hydraulic head (h) are taken as the primary unknowns. The resulting finite-element discretization is given as:

$$F = G_s u \quad (1)$$

$$Q = G_f h \quad (2)$$

where:

$$G_s = \int_V B^T D\, B dV \quad (3)$$

$$G_f = \int_V A^T K\, A dV \quad (4)$$

where:

F is the vector of applied boundary tractions
Q is the vector of boundary discharge
B is the strain-displacement matrix
D is the matrix representing the elastic property of the porous medium
A contains the derivatives of the element shape functions
K is the matrix of hydraulic conductivity

Equations (1) and (2) can be combined in matrix form as:

M. Bai, member SME, is research associate with the School of Petroleum and Geological Engineering, University of Oklahoma, Norman, OK. **D. Elsworth**, member SME, is associate professor with the Department of Mineral Engineering, The Pennsylvania State University, University Park, PA. SME preprint 93–6, SME Annual Meeting, Feb. 14–17, 1993, Reno, NV. Manuscript March 8, 1994. Discussion of this peer-reviewed and approved paper is invited and must be submitted, in duplicate, prior to Oct. 31, 1995.

Table 2 — Optimal production plan for the gold deposit case study

Year	Pit No.	Amount mined, 10^6 tons	Amount milled, 10^6 tons	Metal, 10^3 oz	NPV, $\$x10^6$
1	3	47.88	6.89	565	-152.42
2	5	23.94	10.12	474	-112.76
3	7	35.91	7.74	528	-74.82
4	11	35.91	9.59	437	-62.35
5	13	27.93	8.39	445	-36.24
6	15	23.94	7.05	420	-15.38
7	17	23.94	8.63	399	1.20
8	19	27.93	8.57	412	15.69
9	22	35.91	8.25	380	22.55
10	25	35.91	9.70	317	28.34
11	27	27.93	5.31	208	30.22

1 short ton = 0.91 metric tons, 1 oz = 31.103 grams

Table 3 — Best paths for different mine lives for the gold deposit case study

Mine life, years	Optimal pit sequence	Maximum NPV, $\$x10^6$
1	6	-84.87
2	2-4	-87.78
3	3-5-7	-73.42
4	5-11-15-19	-44.40
5	5-11-15-19-25	-6.23
6	4-7-12-15-18-23	13.21
7	4-7-12-15-18-22-27	25.83
8	4-8-12-14-17-21-25-29	27.77
9	4-8-12-14-17-21-25-29-31	29.74
10	3-5-8-11-13-15-17-19-22-25	28.34
11	3-5-8-11-13-15-17-19-22-25-27	30.22
12	3-5-7-11-13-15-17-19-22-25-28-31	30.13

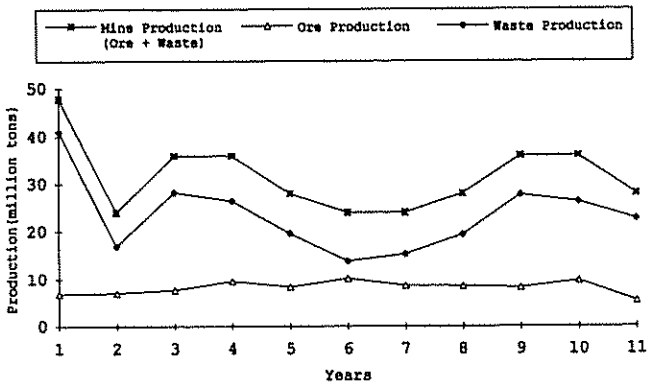

Fig. 5 — Optimum production schedule for the gold deposit case study.

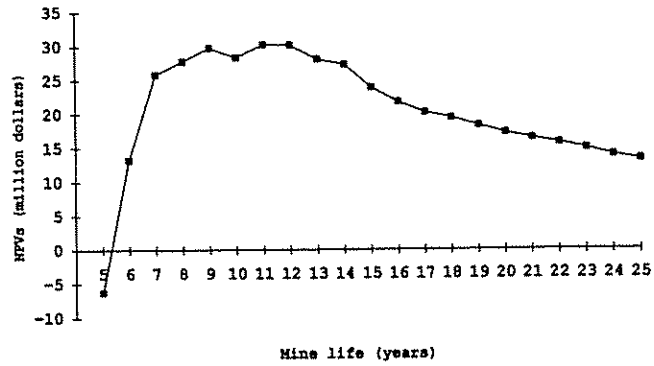

Fig. 6 — The NPVs of the best production planning paths for different mine lives.

searches were conducted for mine lives ranging from 1 to 12 years. All 12 optimal sequences were identical to those of the DP algorithm. Searches beyond a 12-year mine life could not be conducted due to extensive memory requirements of the developed exhaustive search algorithm.

Conclusions

In light of the above discussion, the following conclusions can be made:

- The DP based search algorithm enables the production planning model to function at its fullest capability, and therefore, to bring solutions to real life cases.
- The algorithm uses the most realistic economic decision criteria (NPV) in finding the optimal plan. The NPV calculation is based on the net cash flows (NCF) realized at each arc. The calculation of NCF requires real economic parameters such as capital cost, depreciation, depletion, and taxation. Conventional production planning models resorted to rather simplified NPV calculations.
- Through the application of the algorithm to a real life gold deposit, it has been proven that the optimal production plan cannot be obtained by fixing the mine life or ultimate pit limits as practiced in a number of conventional models.

The following improvements are envisioned for the developed algorithm:

- Incorporate mining and milling constraints and practical operating scenarios to obtain more consistent ore, metal, and waste productions. These constraints and scenarios could be: ore stockpiling, removal of overburden by a contractor, access roads, and working slope.
- Bring a simultaneous solution to the mill cutoff grade together with the rest of the planning parameters.

References

Dohm, G.C., 1979, "Circular analysis — open pit optimization," *Open Pit Mine Planning and Design*, J.T. Crawford and W.A. Hustrulid, eds., SME-AIME, New York, pp. 283-310.

Dreyfus, S.E., and Law, A.M., 1977, *The Art and Theory of Dynamic Programming*, Academic Press, New York, pp. 203.

Wang, Q., 1992, "Open pit production planning through pit-generation and pit-sequencing," unpublished PhD thesis, Southern Illinois University at Carbondale, Carbondale, Illinois, p. 203.

Wang, Q., and Sevim, H., 1993a, "An alternative to parameterization in finding a series of maximum-metal pits for production planning," *Proceedings of the 24th APCOM*, Montreal, Quebec, Canada, Vol. 2, pp. 168-175.

Wang, Q., and Sevim, H., 1993b, "Open pit production planning through pit-generation and pit-sequencing," *Transactions*, Vol. 294, SME, Littleton, CO, pp. 1966-1972.

$$\begin{pmatrix} F \\ Q \end{pmatrix} = \begin{pmatrix} G_s & 0 \\ 0 & G_f \end{pmatrix} \begin{pmatrix} u \\ h \end{pmatrix} \qquad (5)$$

Strata deformation and fluid flow

Equation (5) comprises a diagonal matrix system and therefore, by definition, fluid flow is decoupled from solid deformation. The coupling may be achieved by applying a simple relationship between hydraulic conductivity and solid strain through application of an equivalent porous medium. The parallel plate description is used to represent flow in a fractured reservoir.

Where fracture flow dominates, and only the steady condition is desired, the behavior of the fractured media reduces to that of an equivalent single-porosity medium. Neglecting turbulent flow and assuming only flow within the fracture network, the hydraulic conductivity of a set of parallel fractures of spacing (s) is given as:

$$K = \frac{g\, b^3}{12\, s\, \mu_k} \qquad (6)$$

where:

g is gravitational acceleration
b is initial fracture aperture
s is fracture spacing
μ_k is kinematic viscosity of fluid

Since the aperture of individual fractures will change with solid body strain, the conductivity of the strata will therefore be sensitive to mining induced displacements.

Assuming that the individual fractures are distinctly soft with respect to the porous medium, then the deformation modified conductivity may be written as (Elsworth, 1989):

$$K = \frac{g}{12\, \mu_k s} \left(b + s\Delta\varepsilon\right)^3 \qquad (7)$$

where:

$\Delta\varepsilon$ is the body strain perpendicular to the fracture set.

When the compliance of the elastic matrix approaches that of the fracture, the modulus of the matrix must be included in the evaluation of permeability enhancement. Total displacements are the sum of the elastic displacements in the matrix and across the fracture (shear displacement and dilation are neglected). The total displacement Δu_t resulting from a change in stress ($\Delta\sigma$) is given as:

$$\Delta u_t = \Delta u_s + \Delta u_f = \left(\frac{s}{E} + \frac{1}{K_n}\right) \Delta\sigma \qquad (8)$$

where:

Δu_s and Δu_f are the displacements of the solid and the fracture, respectively
K_n is the normal stiffness of the fracture

The modified permeability of a single fracture set that incorporates solid deformation may be calculated using:

$$\Delta K = \frac{g\, b^3}{12\, \mu_k s} \left[1 + \Delta\varepsilon \left(\frac{K_n b}{E} + \frac{b}{s}\right)^{-1}\right]^3 \qquad (9)$$

The deformation-induced enhancement of permeabilities can be calculated by using Eq. (9) where body strains are evaluated from the finite-element analysis. In many cases, in situ conductivities are available. Therefore, the initial fracture aperture (b_o) may be estimated from Eq. (6) by the following equation in which (K_o) is the initial hydraulic conductivity:

$$b_0 = \left(\frac{12\, \mu_k s\, K_0}{g}\right)^{\frac{1}{3}} \qquad (10)$$

Prediction of surface subsidence

The prediction of surface subsidence by the finite-element technique is subject to various constraints (e.g., material properties may be modified over the actual value in such an extent that the orders of difference may result). More often, a detailed characterization of the effective overburden properties is required including experimental results scaled to reflect mass behavior in the field.

For site-specific case studies using the finite-element approach, it is important that the measured subsidence curve compares favorably with that evaluated by the finite-element calculation. A simple finite-element model is given in Fig. 2 comprising 48 elements and 63 nodes. Due to the symmetry, only half of the mining section is shown. Force boundary conditions are applied both to the immediate roof and floor of the panel in which small moduli are designed to simulate the gob behavior. For comparison, a specific example of longwall mining-induced subsidence is chosen as reported by Moebs and Barton (1985). The isotropic effective elastic modulus is determined that provides the best fit between measured and calculated maximum surface subsidence magnitudes. In this example, the overburden is assumed to be homogeneous. The resulting subsidence profile (illustrated in Fig. 3) indicates that only the maximum subsidence is matched between the measured and calculated (FEM1) distributions. The subsidence trough evaluated by FEM1 appears much flatter compared with the measured trough. This phenomenon reveals that the effective elastic model proposed in this study is inherently stiffer than the actual strata in not admitting degradation in areas of failure. The final subsidence curve in Fig. 3, reported by Moebs and Barton (1985), was obtained 12 months after mining where the overlying strata had been subjected to fracturing and compression. In consequence, the strata would be much more compliant than in the pre-mining state.

To circumvent this situation, a piecewise linear stress-strain relationship may be incorporated. Alternatively, the material partition shown in Fig. 4 enables representation of a softer material over the gob compared to the stiffer strata over the coal pillar $E_3 < E_1 = E_4 < E_2$ as tabulated in Table 1. The effective elastic modulus over the pillar has also been adjusted over the original value ($1.5\, xE_2$). This manipulation reshapes the subsidence curve (FEM2), and yields a good match between the measured and calculated (FEM2) curves, as illustrated in Fig. 3.

Effective elastic modulus exerts a controlling influence over the modeled subsidence magnitude. To further understand this

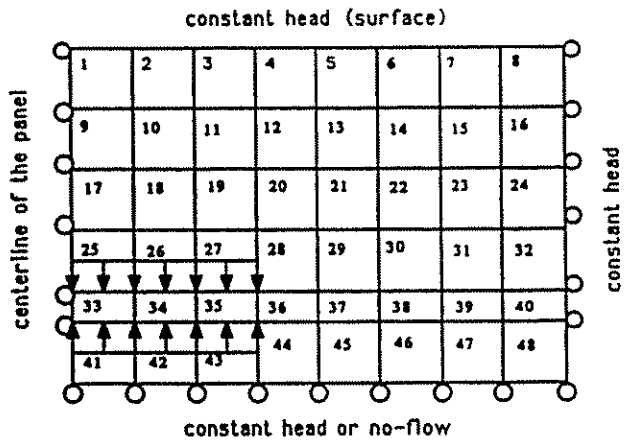

Fig. 2 — Mesh layout of finite-element model.

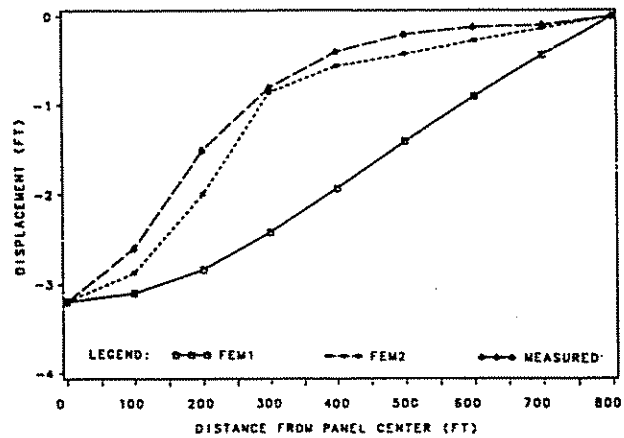

Fig. 3 — Surface subsidence by various methods (FEM1: E = 130,000; FEM2: E1 = 550,000, E2 = 40,000 psf).

mechanism, the study is extended to 13 individual case studies (documented by Moebs and Barton, 1985; Marino, 1988; Hasenfus et al., 1988; Moebs, 1982). The finite-element model is used for all 13 cases, where effective elastic modulus is determined iteratively to match the observed maximum surface subsidence for each case. Since only the matching of maximum subsidence is intended, no partition of effective elastic modulus (assign different moduli to different part of strata) is assigned. The final results are given in Table 2 (L and D represent panel width and depth, respectively). It is of interest to note that the average subsidence factor is only 0.53, representing the shallow but strong overburden in the U. S. coalfields.

Influence of mining under longwall geometry — A case study

The validity of the proposed model may be best illustrated by direct comparison with field measurements taken around a developing longwall panel at a specific mine. The mine is located in West Virginia. Decreasing permeabilities recorded with depth suggest the dominance of secondary porosity (fractures) in determining conductivity magnitudes. The coal seam is approximately 710 ft (216.4 m) deep at the mine (Fig. 5). The mine is located within the Pittsburgh Seam with an average extraction thickness of 5.75 ft (1.75 m). The mined panel is 600 ft (182.9 m) wide by 7200 ft (2194.6 m) long.

The subsidence, measured 17 months after mining on surveying line, is selected for comparison. Substantial subsidence over the seam may be attributed to the impact from

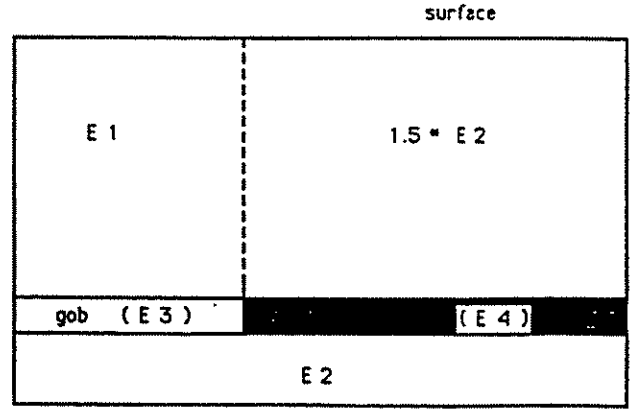

Fig. 4 — Material partition in finite-element model.

Table 1 — Material properties for a finite-element model

Parameter		Strata	Coal seam	Gob
Modulus	(PSf)	130,000	40,000	0.001
	(MPa)	6.22	1.92	0.00
Poisson ratio		0.28	0.30	0.40

adjacent mining. It is noted that the irregular shape of this subsidence curve may be the result of a smaller development pillar on the tailgate side (Fig. 6). A force boundary condition is applied at the seam level to induce elastic deformation in the finite-element model consisting of 429 nodes and 384 elements. As mentioned previously, to match the observed curve by FEM, the strata directly overlying the gob are assumed to consist of softer materials than elsewhere due to the impact of caving. The subsidence curve predicted by one of the influence function methods (Liu et al., 1984) is also plotted in Fig. 6 for comparison. Figure 6 illustrates reasonable agreement between the subsidence predictions from different methods over the gob area.

Figure 7 illustrates the vertical displacement field over the gob. The subcritical nature (i.e., the width to depth ratio of the panel is not sufficiently large to create maximum possible surface subsidence) of the surface subsidence trough can be viewed as the result of a narrowly bounded subsidence domain over the gob. This reflects the effect of caving on the overlying strata. Large vertical displacements are primarily confined to the regions close to the mining level.

Comparison can be made between the measured subsidence contours and the calculated ones. Figure 8 depicts the measured subsidence contours reported by Downdell (Orchard, 1975) that appear qualitatively similar to those evaluated in Fig. 7.

Constant head conditions are maintained at the four boundaries of the model as well as at the periphery of the mining panel. The steady head distribution (resulting from mining) as calculated from the finite-element model is indicated in Fig. 9 where no modification of hydraulic conductivity is assumed. These equipotential lines clearly demonstrate the direction of fluid flow toward the panel. Calculated post-mining hydraulic conductivity distribution in the vertical direction is illustrated in Fig. 10 for an assumed fracture spacing (s) of 0.3281 ft (0.1 m). As anticipated, the greatest change in hydraulic conductivity occurs in the area immediately over the gob where large deformations result. The variation of hydraulic conductivity is strongly dependent upon the assumed fracture spacing and ascribed elastic parameters. It is apparent from Fig. 10 that a dramatic increase

Table 2 — Measured and calculated parameters for subsidence prediction

Case	Width ft	Width m	Depth ft	Depth m	Ratio L/D	Smax ft	Smax m	Smax factor	Modulus E PSf	Modulus E MPa
1	600	183	800	244	0.75	3.20	0.98	NA	130,000	6.22
2	600	183	650	198	0.92	4.40	1.34	NA	117,000	5.60
3	300	91	655	200	0.46	3.00	0.91	NA	60,000	2.87
4	462	141	620	189	0.75	5.20	1.58	0.59	72,600	3.48
5	480	146	585	178	0.82	3.90	1.19	0.60	115,430	5.53
6	450	137	650	198	0.69	2.95	0.90	0.53	150,650	7.21
7	600	183	585	178	1.03	3.28	1.00	0.60	171,585	8.22
8	550	168	350	107	1.43	7.10	2.16	0.71	82,751	3.96
9	440	134	440	134	1.00	7.30	2.23	0.73	66,881	3.20
10	600	183	710	216	0.85	3.58	1.09	0.65	134,400	6.44
11	430	131	375	114	1.15	3.23	0.98	0.50	127,265	6.09
12	380	116	362	110	1.05	1.91	0.58	0.29	268,000	12.83
13	450	137	775	236	0.58	0.94	0.29	0.13	270,000	12.93
Avg.	488	149	581	177	0.88	3.85	1.17	0.53	135,889	6.51

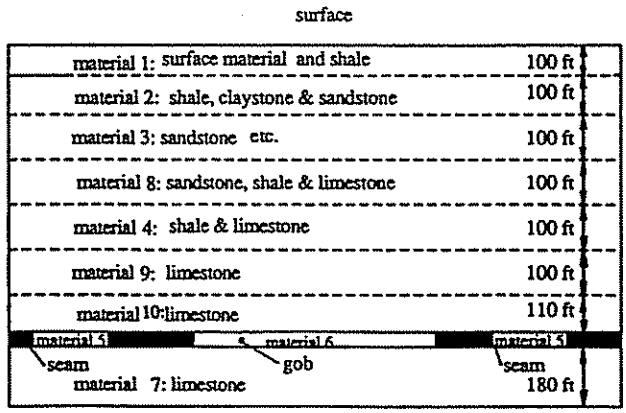

Fig. 5 — Strata lithology (data: Consol, 1990).

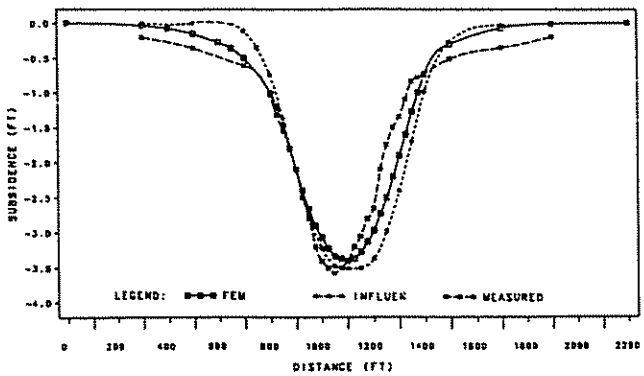

Fig. 6 — Surface subsidence by different methods.

of vertical conductivity occurs in the surface tension zone. This is in contrast to a decrease in the ground compression zone which reflects the influence of tensile and compressive strains in the surface region.

Influence of mining under narrow-face geometry — A parametric study

To minimize the adverse impact on the hydro-geo-mechanical environment as a result of longwall mining, an alternative method (short-longwall mining) is considered. It is important to note that the two methods differ mainly in face width. The selected face width for a short-longwall in our analysis is 200 ft (61 m). Other parameters remain as in the previous section.

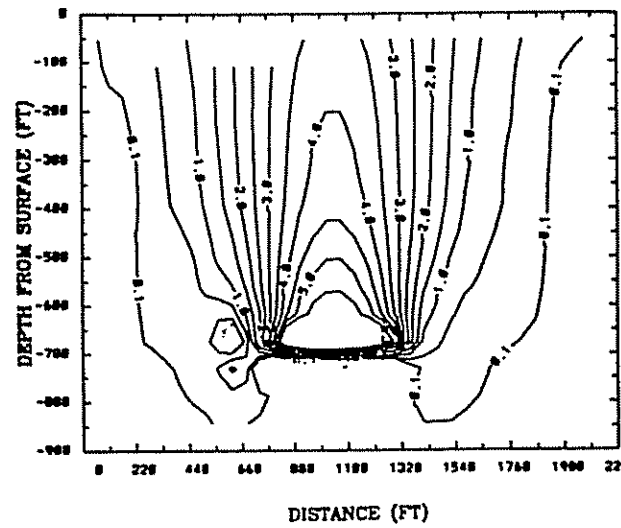

Fig. 7 — Subsidence over longwall panel (ft).

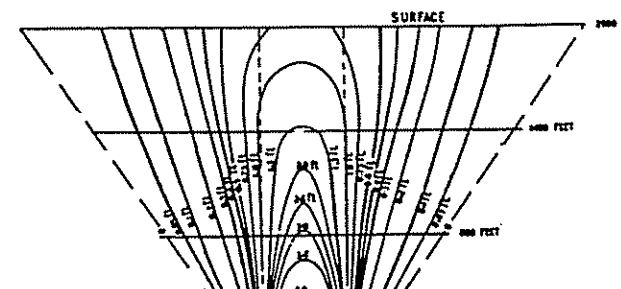

Fig. 8 — Measured subsidence over longwall panel (ft) (after Orchard, 1975).

Impact of mining width

Increased mining width accentuates the intensity of damage in the overlying strata. The decreased severity of strata damage that accompanies short-longwall mining is identified in the following paragraphs.

Subsidence contours for a short-longwall are shown in Fig. 11. The results can be compared directly with those of a full-longwall described previously. The significant difference between the two scenarios may be attributed to

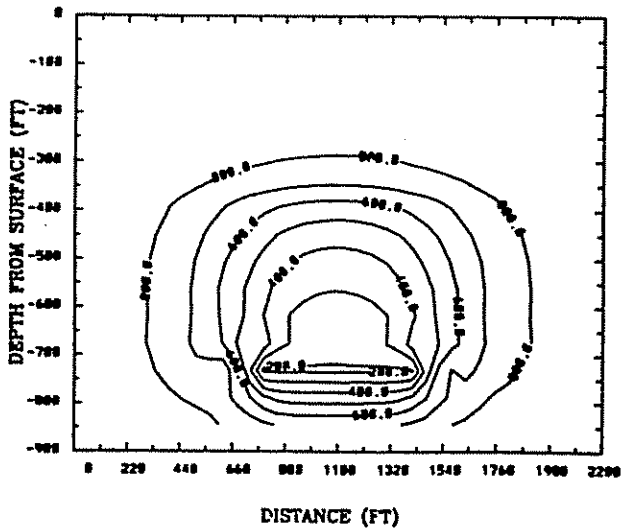

Fig. 9 — Hydraulic head over longwall panel (ft).

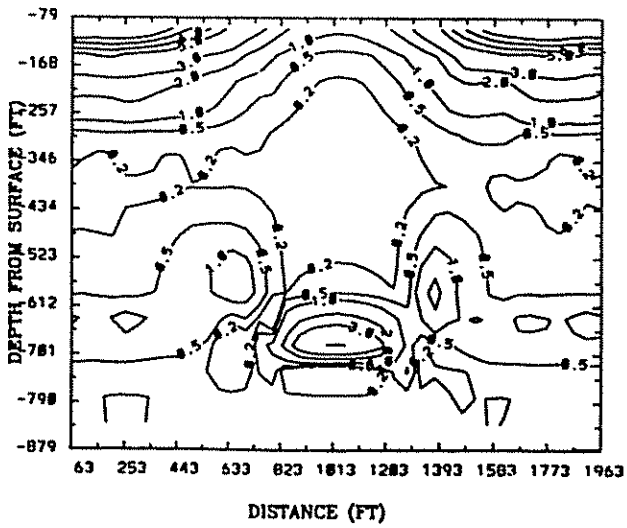

Fig. 10 — Vertical hydraulic conductivity (gpa/ft^2, s = 0.1 m).

the dramatic reduction of surface displacement in short-longwall mining of as much as 80% - 90% of that in conventional longwall mining. It may be noted that the general pattern of displacements by the two methods are quite similar though the extent of strata movement is narrower for the short-longwall due to the decrease of mining width by approximately two-thirds.

The extent of head change is much more localized around the short-longwall panel as illustrated in Fig. 12, in comparison with that of longwall mining (Fig. 9). This reflects the reduced severity of deformations achieved by the short-longwall scheme. Figure 13 depicts the change in vertical conductivity resulting from short-longwall mining where the major disturbance appears merely at the mining level. This is in contrast to the extensive disturbance, both at panel and surface, where longwall extraction is considered.

Multi-panel short-longwall mining

The resultant disturbance due to strata deformation and consequent changes in conductivity in multi-panel mining is expected to be greater than that due to a single panel. A simple example represents a two-panel geometry. Deformation and resulting modification of hydraulic conductivity may be determined for this geometry.

For a two-panel system, Fig. 14 gives the contour lines of

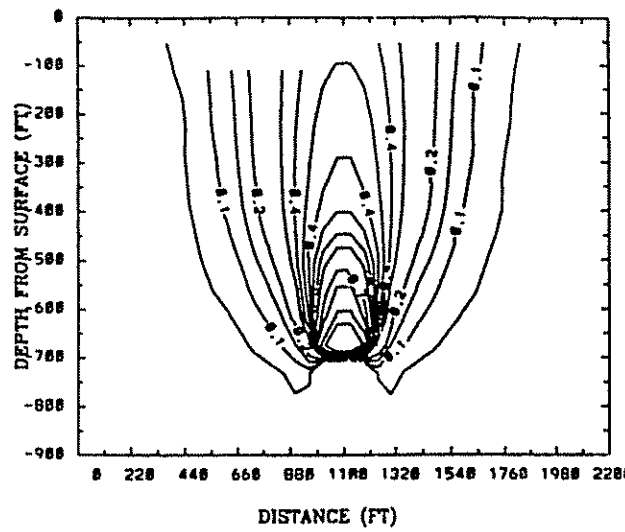

Fig. 11 — Subsidence over short-longwall panel (ft).

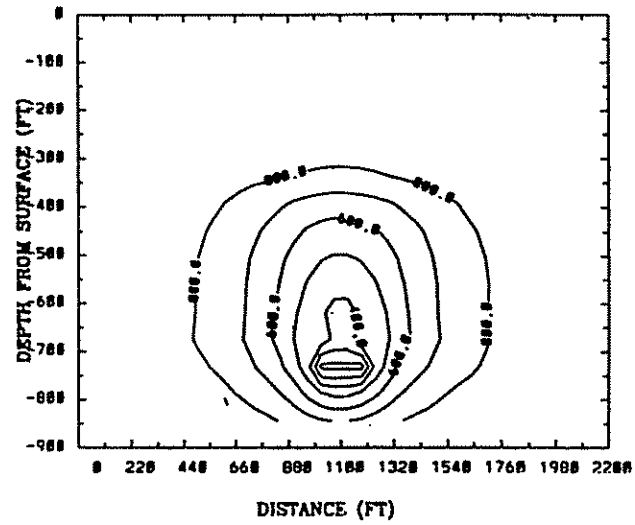

Fig. 12 — Hydraulic head over short-longwall panel (ft).

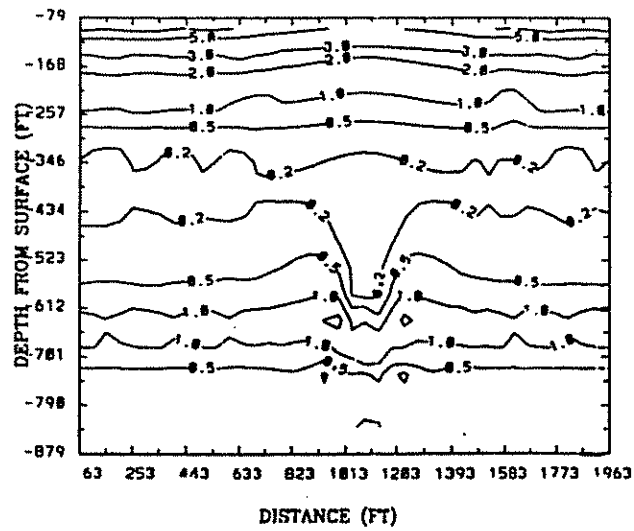

Fig. 13 — Vertical conductivity over short-longwall panel (gpd/ft^2, s = 0.1m).

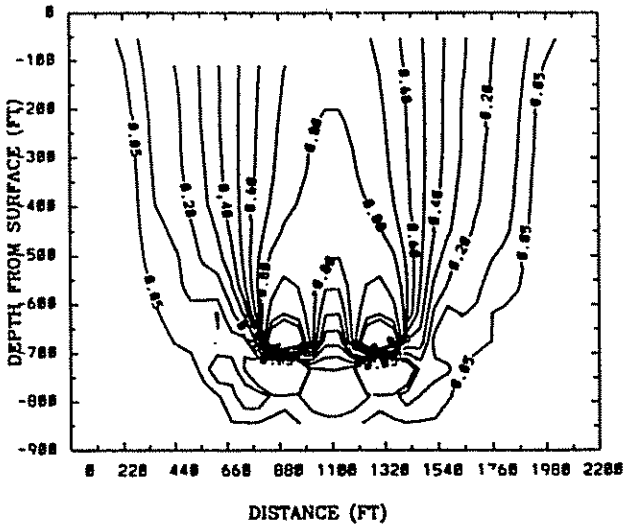

Fig. 14 — Subsidence over short-longwall panel (ft).

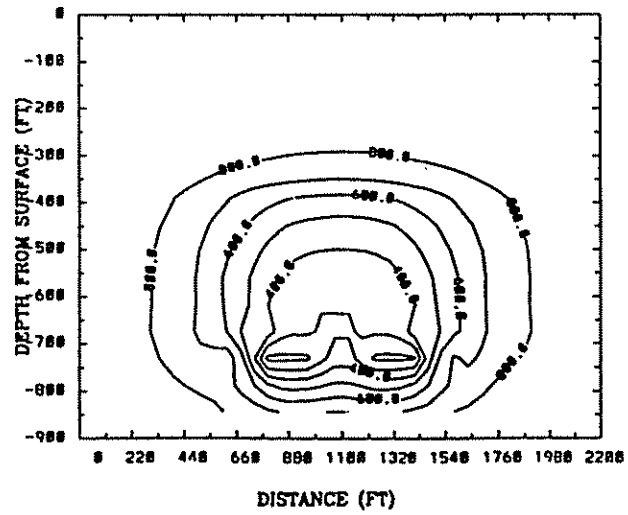

Fig. 15 — Hydraulic head over short-longwall panel (ft).

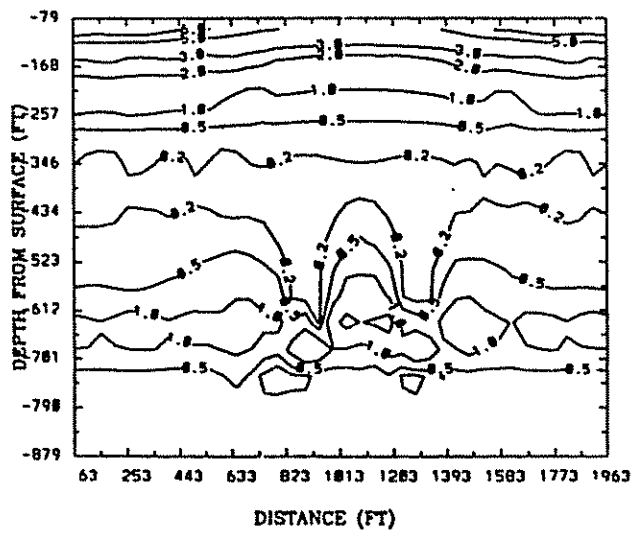

Fig. 16 — Vertical conductivity over short-longwall panel (gpd/ft^2, s = 0.1m).

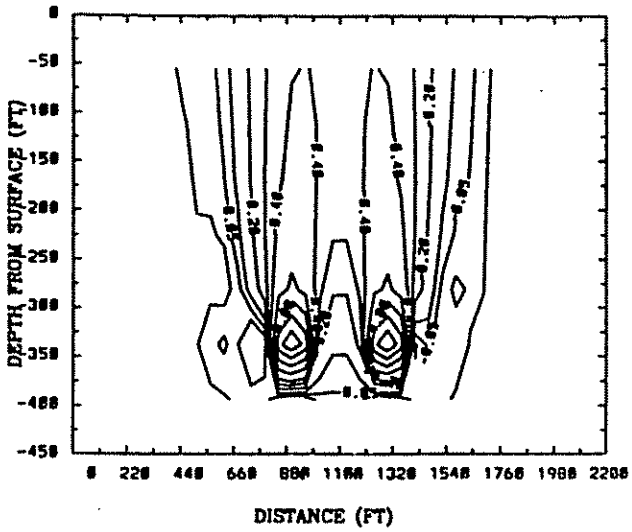

Fig. 17 — Subsidence over shallow short-longwall panel (ft).

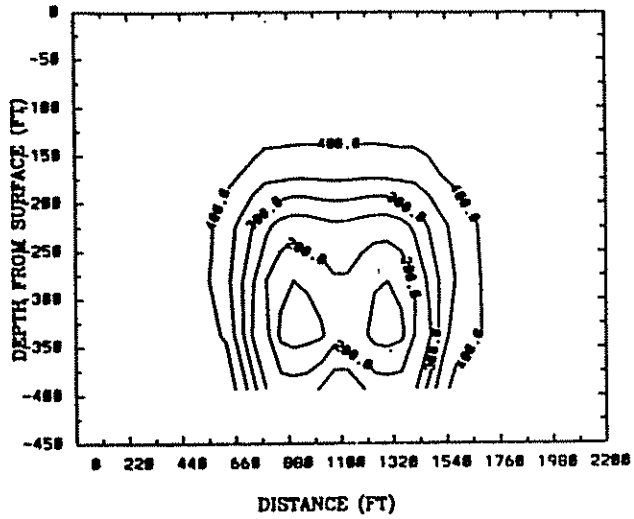

Fig. 18 — Hydraulic head over shallow short-longwall panel (ft).

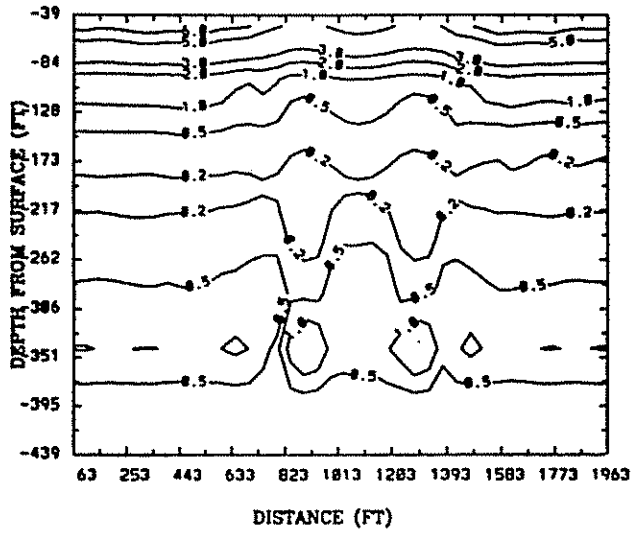

Fig. 19 — Vertical conductivity over shallow short-longwall panel (gpd/ft^2, s = 0.1m).

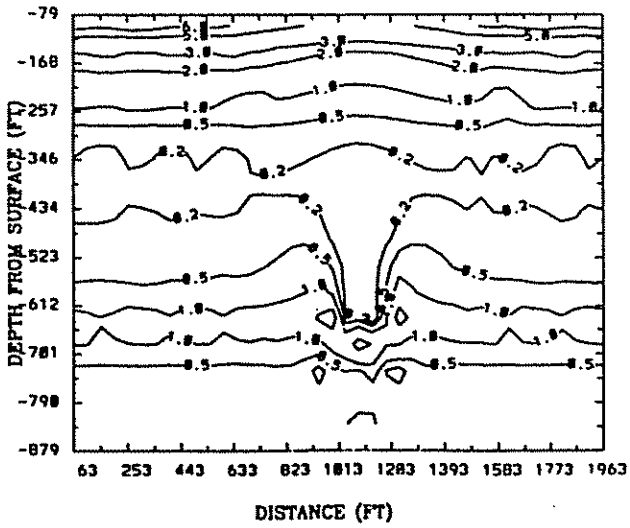

Fig. 20 — Vertical conductivity with fracture spacing 0.01 m (gpd/ft^2, short-longwall).

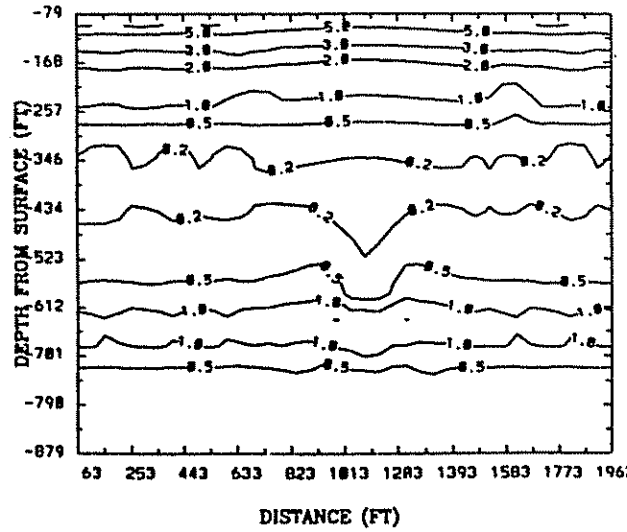

Fig. 21 — Vertical conductivity with fracture spacing 1 m (gpd/ft^2, short-longwall).

subsidence in the overlying strata. To avoid excessive superposition of strains over the barrier pillar, careful consideration should be exercised over the use of yield pillars, increasing pillar size, or reducing mining width.

Figure 15 indicates the head distribution around the two-panel short-longwall scheme. A sharp change in head is observed primarily in the vicinity of the barrier pillar. Vertical conductivity for the two-panel short-longwall system is contoured in Fig. 16 and may be compared with the single-panel scheme in Fig. 13. For all these cases, significant change in hydraulic conductivity is confined to the vicinity of the mining panel for the short-longwall schemes.

Impact of mining depth

The finite-element model with 50% reduction in depth from the previous model is designed to evaluate the impact of mining depth. A two-panel system is analyzed. Figure 17 represents contours of subsidence. In comparison with the two-panel system at greater depth, strata deformation occurs in a narrow region of similar intensity to that for the deeper panel. The hydraulic head distribution is given in Fig. 18. The mining-induced vertical conductivity is given in Fig. 19. It is of interest to note that the influence of mining causes greater modification to the vertical conductivity within the mining region at shallower depth.

Impact of fracture spacing

An equivalent porous medium approximation is used to represent the fractured medium, as identified previously. In the absence of deformation and for a prescribed fracture aperture, conductivity increases proportionally with fracture frequency. In the study, the effect of fracture spacing ranging from 1 cm to 100 cm (0.0328 ft to 3.2808 ft) is investigated for short-longwall mining situations in terms of the variation in vertical conductivity with mining-induced strains.

For the single-panel short-longwall scheme, Fig. 20 indicates the modified vertical conductivity for a fracture spacing of 1 cm (0.0328 ft), with Fig. 21 representing the behavior for a fracture spacing of 1 m (3.2808 ft). It is seen that greater hydraulic conductivity changes occur for the smaller fracture spacings.

Comparison of surface subsidences under various mining geometries

Application of the short-longwall scheme offers significant advantage over longwall mining in terms of its potential to minimize surface subsidence. Figure 22 illustrates the difference in surface subsidence between longwall (width = 600 ft or 183 m) and short-longwall mining (width = 200 ft or 61 m). Subsidence for the short-longwall is approximately one-seventh of that resulting from longwall mining.

Surface subsidence resulting from different short-longwall schemes is depicted in Fig. 23. (Note: "short" represents subsidence due to single-panel short-longwall at shallower depth; "short 1" is subsidence due to two-panel short-longwall at shallower depth; "short 2" indicates subsidence due to two-panel short-longwall at deeper depth.) It appears that depth of mining plays a major role in determining the magnitude of subsidence. Deeper mining results in greater subsidence magnitudes, due to greater accumulative strata compression. In reality, this may not be true due to strata arching mechanism. Therefore, the smaller subsidence may result from deeper mining depth. The present finite-element model cannot predict this scenario.

For identical depth (H = 710 ft or 216.4 m), the maximum subsidence in a two-panel system ("short 2" in Fig. 23) almost doubles the magnitude observed in a single-panel system ("short" in Fig. 22), while the subsidence trough appears much broader compared to the single-panel scheme.

It is also noted that ground heave occurs in the shallower two-panel scheme due to the effect of the barrier pillar. It is expected that higher tensile strains would occur in this region.

Influence of topography

The model described in the preceding is applicable under certain idealized situations. For more complex geometries and strata conditions, additional factors need to be considered. The change in hydraulic conductivity in environments with steep topography is different from those with flat-lying surface topography. Shear displacement along weak planes of major joints frequently results in additional strata movement in the steep terrain. The fluctuation of surface topography within the zone of surface influence may vary signifi-

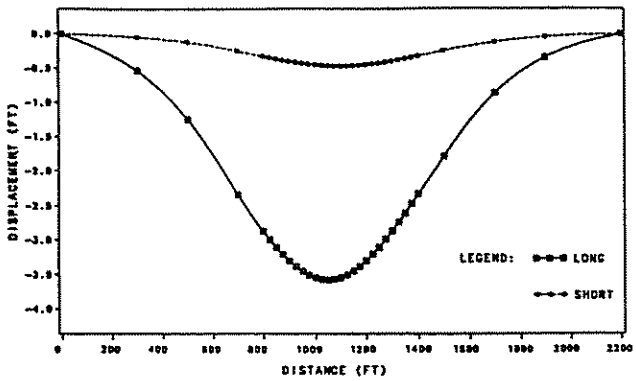

Fig. 22 — Subsidence by longwall and short-longwall mining.

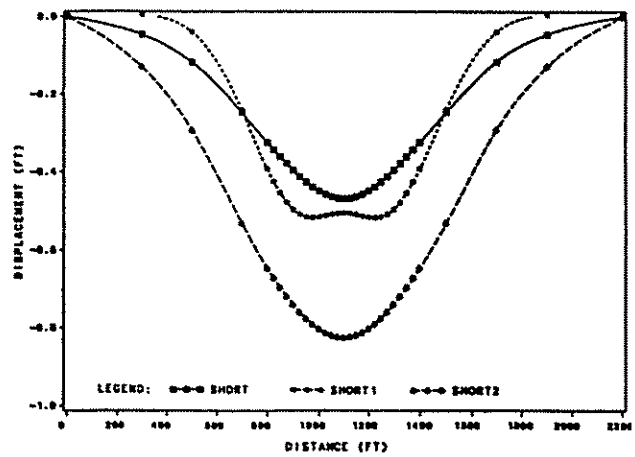

Fig. 23 — Subsidence by various short-longwall schemes.

cantly, resulting in modification of the initial stress distribution and flow boundary conditions.

Contrast of hydraulic conductivities

To increase the contrast of hydraulic conductivities between different layers in a finite-element analysis, a finer mesh is required in order to accurately represent the sharp change of hydraulic conductivity at the layer interface. This measure is particularly important in representing composite layers of shalestone and sandstone due to the substantial difference in their hydraulic conductivities.

A significant contrast of hydraulic conductivities in the horizontal and vertical directions may exist due to rock anisotropy. Permeability contrasts of 10:1 are not uncommon and may reach 100:1 in the coal measure rocks. Anisotropic permeability should be accommodated within individual strata where it is necessary.

Concluding remarks

Coupling elastic deformation and fluid flow in determining the steady response to mining has been obtained from an equivalent porous medium model. This simplified coupling shows that strata deformation has a controlling influence over changes in hydraulic conductivity. The principal changes occur in the vicinity of the mining panel where excessive strains due to mining are expected. Smaller changes are apparent in the tension zone close to the ground surface.

The case study shows that the change in hydraulic conductivity within or adjacent to shallow aquifers over longwall mining panels may be associated with strata tensile strains induced by deep mining. The maximum hydraulic conductivity within the zone of strong influence is increased by about tenfold over the pre-mining level (Hasenfus et al., 1988).

Narrowing the face width significantly reduces the structural damage to overlying strata by mining. However, leaving a relatively wide barrier pillar between the short face panels may cause the undesirable superposition of tensile strains over the pillar. From the preceding analysis, a reduction of face width by two-thirds results in a 50% - 80% reduction in strata deformation, and narrows the region of dramatic hydraulic head change. This subsequently confines the change of hydraulic conductivities to the mining area, thus minimizing the influence of mining on surface or near-surface strata.

Comparison between multi-panel and single-panel schemes indicates that a significant increase in the magnitude as well as in the extent of mining influence occurs for the multi-panel system.

Acknowledgements

This work was supported in part by the National Land Reclamation Center under grant CO 388026 and the Pennsylvania Energy Department Authority. Field data and useful suggestions offered by personnel of the Consolidation Coal Company Research and Development Office are gratefully acknowledged.

References

Bai, M., 1991, "Numerical models of fluid flow and solid deformation in fluid saturated media," PhD Thesis, The Pennsylvania State University.

Booth, C.J., 1984, "A numerical model of groundwater flow associated with an underground coal mine in the Appalachian plateau, Pennsylvania," PhD Thesis, The Pennsylvania State University.

Elsworth, D., 1989, "Thermal permeability enhancement of blocky rocks: one-dimensional flows," *International Journal of Rock Mechanics, Mineral Science and Geomechanical Abstracts*, Vol. 26, No. 3/4, pp. 329-339.

Hasenfus, G.J., Johnson, K.L., and Su, D.W.H., 1988, "A hydrogeomechanical study of overburden aquifer response to longwall mining," *Proceedings*, 7th International Conference on Ground Control in Mining, Morgantown, WV, pp. 149-162.

Liu, T., et al., 1984, "Coal mine ground movement and strata failure," *China Coal Ministry Publishing Company.*

Marino, G.G., 1988, "Analysis of the initial collapse of the overburden over longwall panels using subsidence data," *Proceedings*, 7th International Conference on Ground Control in Mining, Morgantown, WV, pp. 234-246.

Moebs N.N., and Barton T. G., 1985, "Short-term effects of longwall mining on shallow water sources," Bureau of Mines Information Circular, IC 9042, pp. 13-24.

Moebs, N.N., 1982, "Subsidence over four room and pillar sections in Southwestern Pennsylvania," Bureau of Mines Report, RI 8645.

Orchard, R.J., 1975, "Working under bodies of water," *The Mining Engineer*, pp. 261-270.

Owili-Eger, A.S.C., 1975, "Mathematical modeling and digital simulation of soil-aquifer groundwater motion and mine water drainage," PhD Thesis, The Pennsylvania State University.

Walker, J.S., 1988, "Case study of the effects of longwall mining induced subsidence on shallow groundwater sources in the Northern Appalachian coalfields," Bureau of Mines Report, RI 9198.

Methodology for physical characterization of mining-generated and laboratory-generated coal dust particles

J. Li and J.M. Mutmansky

Abstract — *The objective of this study was to produce coal dusts for laboratory research that are similar to mine airborne dusts in chemical, mineral, and physical characteristics. In this investigation, dusts produced in laboratory comminution equipment were compared with continuous-miner-generated dust for similarity in physical characteristics. Mining-generated dust (MGD) and bulk coal samples were first collected from an underground mining operation. The bulk samples were then processed in the laboratory for size reduction in various comminution devices. These laboratory-generated dust (LGD) samples were subjected to size and microscopic analyses. Physical properties of the dust particles were studied on a scanning electron microscope (SEM). A numerical shape coordinate system (SCS) was also developed and applied to 300 particles from each sample. Statistical analysis was then performed on the collected data and characteristics of the MGD and LGD samples were compared.*

Introduction

In many biomedical studies, researchers routinely introduce a dust mass into an experimental environment to assess the response of a biological entity, usually lung macrophages in vitro or a live laboratory animal, to the dust mass. To provide data of maximum usefulness, it is highly desirable to use dust with characteristics of actual mine airborne dust. The primary objective of this research was to produce dusts in the laboratory similar in chemical, mineralogical, and physical characteristics to mine airborne dusts. This paper outlines the evaluation of the physical characteristics of the lab-generated dusts.

Particle shape analysis is perhaps the least-developed area in mineral-related particle science and technology. There are still no standard methods or instruments to scientifically quantify particle shapes. To date, many attempts have been made to characterize particle shapes. These procedures can be roughly classified into three categories:

- methods using linguistic descriptors,
- methods using standard shape comparators, and
- methods using computer-assisted mathematical techniques.

Linguistic descriptors have been widely employed both historically and currently because of their simplicity and convenience. When this method is used for shape representation, particles are often described as "rounded," "blocky," or "needle-shaped," etc. It is clear that the meaning of a linguistic descriptor depends largely on the reader's experience and perception and that the descriptions may be different from one reader to another.

Researchers seeking better shape descriptors have explored methods using shape comparators. To utilize a shape comparator, a shape standard is generally defined first and then particle profiles of interest are compared with this standard. While the shape comparators have some shortcomings, they are relatively easy to apply in shape determination problems and hence are commonly utilized.

The third methodology of shape analysis utilizes mathematical techniques and computer programs for particle shape digitization and data processing. A particle profile is normally converted into a set of coordinates and then shape coefficients are obtained through a series of mathematical transformations. This methodology provides several advantages but has been used primarily for research purposes because the required instrumentation is relatively expensive.

While many different capabilities of a shape analysis method may be sought, the most desirable goals are the ability to differentiate samples where a valid difference exists, efficiency in terms of cost and time, and a facility for visualizing the original particle shape. So far, no method has met all of the above criteria.

Development of a shape coordinate system (SCS)

The SCS system implemented here is based on the geometrical comparator described by Beddow (1980, 1980a). The geometrical comparator chart of Beddow is shown in Fig. 1. The construction of the geometrical comparator can be summarized as follows:

- The baseline of the comparator consists of a set of equidimensional regular figures of 3, 4, 5, 6, 7, 8 and an infinite number of sides or a circle. These are the basic shapes.

J. Li and **J.M. Mutmansky**, members SME, are mining engineer with Resource Enterprises, Inc., Salt Lake City, UT, and professor with the Department of Mineral Engineering, the Pennsylvania State University, University Park, PA, respectively. SME nonmeeting paper 93-324. Manuscript Nov. 8, 1993. Discussion of this peer-reviewed and approved paper is invited and must be submitted, in duplicate, prior to Oct. 31, 1995.